JACS
JOURNAL OF THE AMERICAN CHEMICAL SOCIETY

ARTICLE

pubs.acs.org/JACS

NMR Detection of pH-Dependent Histidine−Water Proton Exchange Reveals the Conduction Mechanism of a Transmembrane Proton Channel

Fanghao Hu, Klaus Schmidt-Rohr, and Mei Hong*

Department of Chemistry, Iowa State University, Ames, Iowa 50011, United States

Supporting Information

ABSTRACT: The acid-activated proton channel formed by the influenza M2 protein is important for the life cycle of the virus. A single histidine, His37, in the M2 transmembrane domain (M2TM) is responsible for pH activation and proton selectivity of the channel. Recent studies suggested three models for how His37 mediates proton transport: a shuttle mechanism involving His37 protonation and deprotonation, a H-bonded imidazole−imidazolium dimer model, and a transporter model involving large protein conformational changes in synchrony with proton conduction. Using magic-angle-spinning (MAS) solid-state NMR spectroscopy, we examined the proton exchange and backbone conformational dynamics of M2TM in a virus-envelope-mimetic membrane. At physiological temperature and pH, ^{15}N NMR spectra show fast exchange of the imidazole ^{15}N between protonated and unprotonated states. To quantify the proton exchange rates, we measured the ^{15}N T_2 relaxation times and simulated them for chemical-shift exchange and fluctuating N−H dipolar fields under ^{1}H decoupling and MAS. The exchange rate is 4.5×10^5 s^{-1} for Nδ1 and 1.0×10^5 s^{-1} for Nε2, which are approximately synchronized with the recently reported imidazole reorientation. Binding of the antiviral drug amantadine suppressed both proton exchange and ring motion, thus interfering with the proton transfer mechanism. By measuring the relative concentrations of neutral and cationic His as a function of pH, we determined the four pK_a values of the His37 tetrad in the viral membrane. Fitting the proton current curve using the charge-state populations from these pK_a's, we obtained the relative conductance of the five charge states, which showed that the +3 channel has the highest time-averaged unitary conductance. At physiologically relevant pH, 2D correlation spectra indicated that the neutral and cationic histidines do not have close contacts, ruling out the H-bonded dimer model. Moreover, a narrowly distributed nonideal helical structure coexists with a broadly distributed ideal helical conformation without interchange on the sub-10 ms time scale, thus excluding the transporter model in the viral membrane. These data support the shuttle mechanism of proton conduction, whose essential steps involve His−water proton exchange facilitated by imidazole ring reorientations.

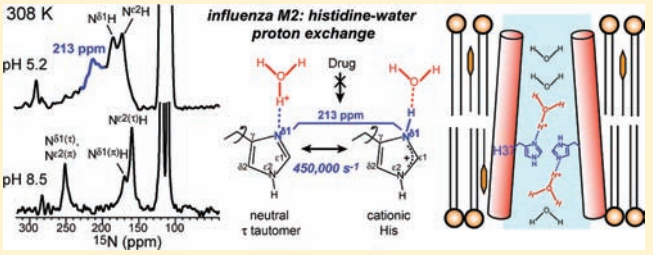

INTRODUCTION

The M2 protein of the influenza virus forms a proton-selective tetrameric channel that allows virus entry into host cells and prevents premature conformational changes of hemagglutinin by maintaining the high pH of the trans-Golgi network.[1,2] M2 also mediates membrane scission and virus budding from the host cell.[3,4] During virus entry, M2 is activated by the low pH of the endosome and conducts 10^1−10^4 protons per second into the virion,[5,6] which causes uncoating and release of the ribonucleoprotein into the host cell. A single residue, His37, in the transmembrane domain (TM) (Figure 1a) is responsible for pH activation and proton selectivity of the channel.[7,8] The channel is irreversibly inhibited by the antiviral drugs amantadine (Amt) and rimantadine,[9] which bind specifically to the TM pore.[10−13] The high-resolution structure of the M2 transmembrane domain (M2TM) has been extensively studied by solid-state NMR (SSNMR) spectroscopy,[10,14,15] X-ray crystallography[11,16] and solution NMR spectroscopy[17] under a range of pH and drug-binding conditions.

Two general mechanisms of proton conduction have been proposed for M2. The water wire model posits that protons are conducted solely by the Grotthuss mechanism[18] via a continuous column of H-bonded water molecules when electrostatic repulsion of several cationic His37's removes the pore constriction at this site (Figure 1b).[19−21] His37 plays a passive role in this model and is not directly involved in the proton transfer. A second model posits that protons bind and unbind His37 with every conduction event, causing His37 conformational changes in the process (Figure 1c).[22] This "shuttle" model was proposed to explain the measured deuterium isotope effect, pH dependence of the proton current, and saturation conductance of the channel.[6,22] We recently reported low-pH specific His37 side-chain reorientation,[23] whose minimum energy barrier of 60 kJ/mol is consistent with the proton conduction barrier of ∼100 kJ/mol obtained from functional assays,[5] supporting the shuttle model.

Received: August 28, 2011
Published: October 05, 2011

dx.doi.org/10.1021/ja2081185 | J. Am. Chem. Soc. 2012, 134, 3703−3713

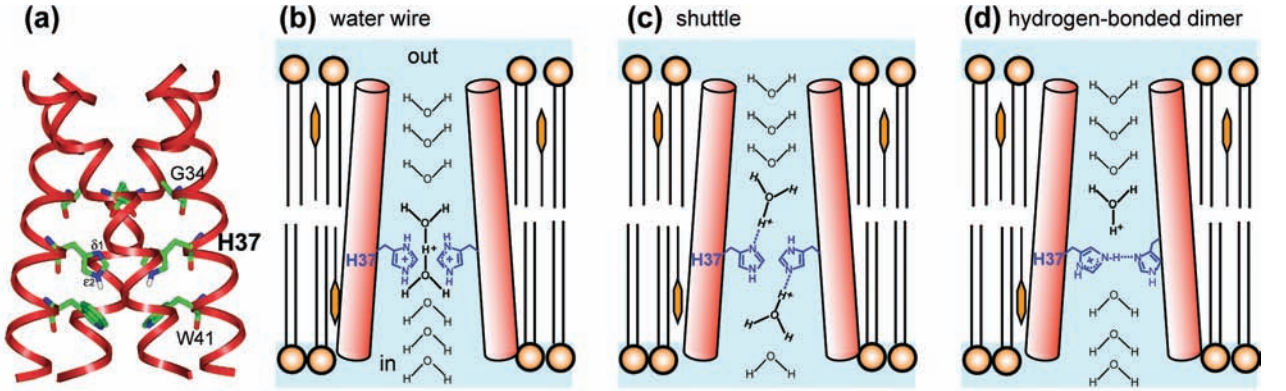

Figure 1. Contending models of the proton conduction mechanism of the influenza M2 proton channel. (a) High-resolution (1.65 Å) crystal structure of the tetrameric M2TM at an intermediate pH of ~6.5 (PDB entry 3LBW). The key residues His37, Trp41, and Gly34 are shown as sticks. (b–d) Schematic illustrations of three proton conduction models. For clarity, only two of the four helices are depicted. (b) The water wire model posits that protons are conducted exclusively by water molecules without involving His37, whose only function is to open the pore constriction at this juncture. A Zundel cation ($H_5O_2^+$) is depicted here as an example of a possible conducting species.[48] The actual water molecules may not be in single file and likely have orientational disorder. (c) The shuttle model posits that protons bind and unbind His37 and that the conformational changes of His37 required to regenerate the initial state for the next proton relay represent the rate-limiting step of proton conduction. (d) The H-bonded dimer model posits that a neutral His37 forms a strong H-bond with a cationic His37 at intermediate pH. The breaking of this H-bond by a hydronium ion causes a His37–Trp41 interaction and subsequent proton transfer to the virus interior.

On the other hand, the energy barrier for purely water-mediated proton transport in M2 was calculated to be less than 42 kJ/mol,[20] suggesting that protons are not solely conducted by a water wire. These results suggest that His37 shuttles protons into the virion by imidazole protonation and deprotonation facilitated by ring reorientation.

Concurrently, two other His-based proton conduction models were also proposed. The H-bonded dimer model, developed on the basis of molecular dynamics (MD) simulations of the His37 structure and interaction with Trp41,[15] suggests a low-barrier H-bond between Nδ1 of a neutral His and Nε2H of a cationic His in the +2 tetrad (Figure 1d). The third protonation event, with a pK_a of 6.3 based on ^{15}N NMR analysis of DMPC/DMPG-bound M2TM,[24] is hypothesized to disrupt this imidazole–imidazolium dimer and establish cation–π interactions between His37 and Trp41. Subsequent conformational fluctuations are envisioned to break this cation–π interaction, exposing Nε2H to the C-terminal water and causing proton transfer.[15] Finally, a transporter model was proposed in which the M2TM backbone alternates between two or more conformations with different water accessibilities to the exterior and interior of the virus, with the motion being synchronized with proton transport.[25,26] This model was based on experimental[11,16,17] and MD-simulated[25] M2 structures showing pH-dependent changes of the tilt angles of the N- and C-terminal halves of the TM helix.

Evaluating these proton conduction models is important not only for influenza virology but also for understanding other ion channels such as voltage-gated proton channels.[27] In this study, we investigated the proton exchange of His37 at physiologically relevant pH, temperature, and membrane composition using magic-angle-spinning (MAS) SSNMR spectroscopy. ^{15}N chemical shift spectra show definitively that His37 is protonated and deprotonated at rates of $\sim 10^5\ s^{-1}$ without the formation of imidazole–imidazolium dimers. We determined the four acid dissociation constants in the virus-envelope-mimetic (VM) membrane,[28] from which the relative conductances of the different charge states of the channel were estimated. These data show that His37–water proton transfer facilitated by imidazole ring reorientation is the essential proton transport mechanism of M2.

MATERIALS AND METHODS

Membrane Sample Preparation. The TM (residues 22–46, SSDPLVVAASIIGILHLILWILDRL) of the M2 protein of the Udorn strain of the influenza A virus was synthesized (PrimmBiotech, Cambridge, MA) using Fmoc solid-phase protocols and purified to >95% purity. The peptide was uniformly ^{13}C,^{15}N-labeled at Gly34, His37, and Ile39 or Ile42.

A VM membrane mixture containing 1,2-dipalmitoyl-*sn*-glycero-3-phosphocholine (DPPC), 1,2-dipalmitoyl-*sn*-glycero-3-phosphoethanolamine (DPPE), egg sphingomyelin (SM), and cholesterol (Chol) was prepared at an SM:DPPC:DPPE:Chol molar ratio of 28:21:21:30.[28] The VM mixture resembles the virus-envelope lipid composition and enhances the spectral resolution of M2TM relative to model phosphocholine bilayers. Importantly, the VM membrane mixture also immobilizes the uniaxial diffusion of the four-helix bundle,[28–30] thus enabling detection of side-chain motions. SM was dissolved in 5:1 chloroform/methanol solution and then mixed with DPPC, DPPE, and Chol in chloroform. The solution was dried with a stream of nitrogen gas, suspended in cyclohexane, and lyophilized. The dry lipid powder was resuspended in 1 mL of buffer solution of the desired pH, vortexed, and freeze–thawed eight times to create uniform lipid vesicles. M2TM powder was codissolved with the detergent octyl-β-D-glucoside (OG) in 1 mL of the same buffer at an OG concentration of 20 mg/mL. The pH of the M2TM/OG solution was adjusted with ~100 μL of dilute HCl or NaOH solution to the desired pH. The solution was then mixed with 1 mL of lipid vesicle solution, vortexed for 2 h, and dialyzed with a 3.5 kDa molecular weight cutoff against 1 L of buffer at 4 °C for 3 days to remove the detergent. The protein–lipid precipitant usually appeared after 1 day. The proteoliposome solution was centrifuged at 150000*g* and 6 °C for 4 h to yield a membrane pellet with a hydration level of ~40 wt %. The final protein:lipid molar ratio was 1:15. The pellet was packed into 4 mm MAS rotors for SSNMR experiments.

Membrane samples were prepared at five pH values from 8.5 to 4.5. The pH 8.5 sample was prepared using a Tris buffer (10 mM Tris, 1 mM EDTA, and 0.01 mM NaN_3). The pH 7.0 sample was prepared using a phosphate buffer (10 mM NaH_2PO_4/Na_2HPO_4, 1 mM EDTA, and 0.01 mM NaN_3). The pH 6.0 sample was prepared using a Bis-Tris buffer (10 mM Bis-Tris, 1 mM EDTA, and 0.01 mM NaN_3). The pH 5.2

dx.doi.org/10.1021/ja2081185 |*J. Am. Chem. Soc.* 2012, 134, 3703–3713

and pH 4.5 samples were prepared using a citrate buffer (10 mM citric acid/sodium citrate, 1 mM EDTA, and 0.01 mM NaN_3). We also prepared two Amt-bound M2TM samples at pH 6.0 and 5.2 by directly titrating 5−7 μL of Amt-containing solution into the NMR rotor to achieve a final drug:tetramer ratio of 4:1. All buffer pH's were measured at ambient temperature, and the pH of the supernatants after centrifugation was checked and verified to be within 0.1 unit of the desired pH.

Solid-State NMR Spectroscopy. SSNMR experiments were carried out on Bruker DSX-400 MHz (9.4 T) and AVANCE 600 MHz (14.1 T) spectrometers (Karlsruhe, Germany) using 4 mm triple-resonance MAS probes. Typical radiofrequency (rf) pulse lengths were 5 μs for ^{13}C, 6−7 μs for ^{15}N, and 3.5−4 μs for ^{1}H. ^{13}C chemical shifts were referenced to the α-Gly CO signal at 176.49 ppm on the tetramethylsilane (TMS) scale, and ^{15}N chemical shifts were referenced to the ^{15}N signal of *N*-acetylvaline at 122.0 ppm on the liquid ammonia scale.

One-dimensional (1D) ^{15}N cross-polarization (CP) MAS spectra were measured using ^{1}H spin-lock field strengths of $\omega_1/2\pi$ = 50 kHz. Unprotonated nitrogens, whose concentrations at different pH values are important for determining the His37 pK_a's, generally have lower CP efficiencies than the protonated nitrogens because of their weak ^{1}H−^{15}N dipolar couplings. To maximize the unprotonated ^{15}N signal, we used a relatively long CP contact time of 3 ms and optimized the Hartman−Hahn condition by using the model compound N-t-Boc-proline, which contains an unprotonated ^{15}N. While the optimal CP contact time for maximizing the unprotonated ^{15}N signal is likely longer than 3 ms, longer contact times reduce the protonated ^{15}N intensity as a result of ^{1}H $T_{1\rho}$ relaxation. Thus, 3 ms was chosen as a compromise. For the pK_a analysis, where quantitative intensity ratios of the NH and N peaks were required, we used neutral His as the model compound to calibrate the scaling factor κ between the NH and N intensities.

^{15}N T_2 relaxation times were measured at 308 K under 7 kHz MAS using a Hahn echo sequence with a 12 μs 180° pulse. The ^{1}H decoupling field strength was 62.5 kHz during the echo delays for all samples to ensure that the motion was probed on the same time scale.

Two-dimensional (2D) ^{1}H-driven ^{13}C spin diffusion experiments with a DARR[31] mixing time of 40−60 ms were conducted under 7−10 kHz MAS. 2D ^{15}N−^{13}C correlation spectra were measured using a REDOR-based pulse sequence[32] for ^{13}C−^{15}N polarization transfer. The experiments were conducted at 273 or 243 K under 7−10 kHz MAS. A typical ^{13}C−^{15}N recoupling time of 0.6 ms was used to obtain one-bond ^{15}N−^{13}C cross-peaks. 2D ^{13}C−^{1}H dipolar chemical shift (DIPSHIFT) correlation experiments[33] were carried out under 3.7, 3.9, and 5 kHz MAS at 308 K. ^{1}H homonuclear decoupling was achieved using the MREV-8 sequence[34] at 3.7 and 3.9 kHz MAS and the FSLG sequence[35] at 5.0 kHz MAS. The ^{1}H 90° pulse length in these homonuclear decoupling sequences was 4 μs. The t_1 time-domain data were fit to obtain the apparent ^{13}C−^{1}H dipolar couplings and then divided by the scaling factor of the homonuclear decoupling sequence (0.47 for MREV-8 and 0.577 for FSLG) to obtain the true couplings.

In measurements of dipolar order parameters, both the homonuclear decoupling scaling factor and the rigid-limit coupling have uncertainties that can affect the values of the order parameters. Thus, we measured the product of these two factors using the crystalline model peptide formyl-Met-Leu-Phe (f-MLF). Using the theoretical scaling factors for MERV-8 and FSLG, we obtained apparent rigid-limit values of 22.7 kHz for the Cα−Hα coupling and high order parameters of 0.95−1.0 for the f-MLF backbone. We used these scaling factors and rigid-limit couplings to extract the His37 order parameters.

Numerical Simulations of ^{15}N T_2 Relaxation under Exchange and ^{1}H Decoupling. ^{15}N T_2 relaxation was simulated using the exchange-matrix formalism,[36] which involves an exchange matrix, a chemical shift matrix, and a dipolar coupling matrix. The 2 × 2 exchange matrix $\vec{\pi}$ has diagonal elements equal to $-k$ and off-diagonal elements equal to $+k$, where $k = {}^{1}/_{2}\tau_C$. The diagonal chemical shift and dipolar

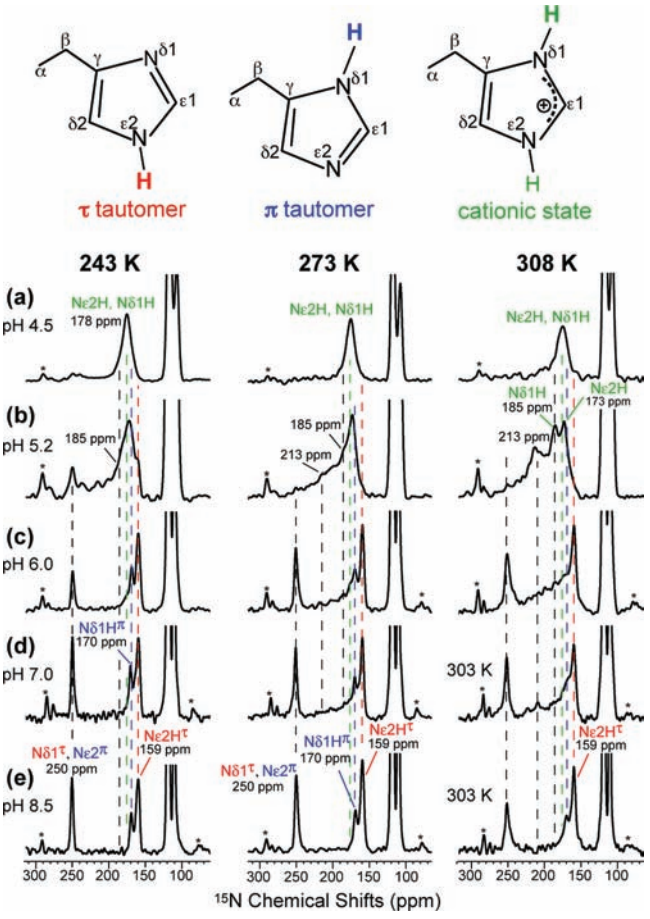

Figure 2. ^{15}N CP-MAS spectra of His37-labeled M2TM as functions of pH and temperature. Peak assignments for the Nε2-protonated τ tautomer (red), Nδ1-protonated π tautomer (blue), and cationic His (green), whose structures are shown at the top, were obtained from 2D correlation spectra. (a) pH 4.5. (b) pH 5.2. (c) pH 6.0. (d) pH 7.0. (e) pH 8.5. Spectra were measured at 243, 273, and 308 or 303 K. The exchange intensities at pH 5.2 and 6.0 above 273 K should be noted. Asterisks indicate MAS sidebands.

coupling matrices have diagonal elements given by eqs 1a and 1b, respectively:

$$\omega_{CS,nn} = \omega_{iso,n} + C_{1,CSA,n}\cos(\omega_r t + \gamma_n) + C_{2,CSA,n}\cos(2\omega_r t + 2\gamma_n) \quad (1a)$$

$$\omega_{NH,nn} = C_{1,NH,n}\cos(\omega_r t + \gamma_n) + C_{2,NH,n}\cos(2\omega_r t + 2\gamma_n) \quad (1b)$$

In eq 1a, $\omega_{iso,n}$ is the isotropic chemical shift frequency of site n and the coefficients $C_{1,CSA,n}$ and $C_{2,CSA,n}$ are given by

$$C_{1,CSA,n} = -\frac{\delta_{CSA,n}}{\sqrt{2}}\sin 2\beta \quad (2a)$$

$$C_{2,CSA,n} = -\frac{\delta_{CSA,n}}{2}\sin^2\beta \quad (2b)$$

The coefficients $C_{1,NH,n}$ and $C_{2,NH,n}$ in eq 1b are defined similarly in terms of the dipolar coupling constants $\delta_{NH,n}$, which include a factor of 2π.

Time was incremented in steps of the dipolar-decoupling pulse spacing $t_{ps} = (2\nu_1)^{-1}$, where $\nu_1 = \gamma B_1/2\pi$ is the radiofrequency field

dx.doi.org/10.1021/ja2081185 |J. Am. Chem. Soc. 2012, 134, 3703–3713

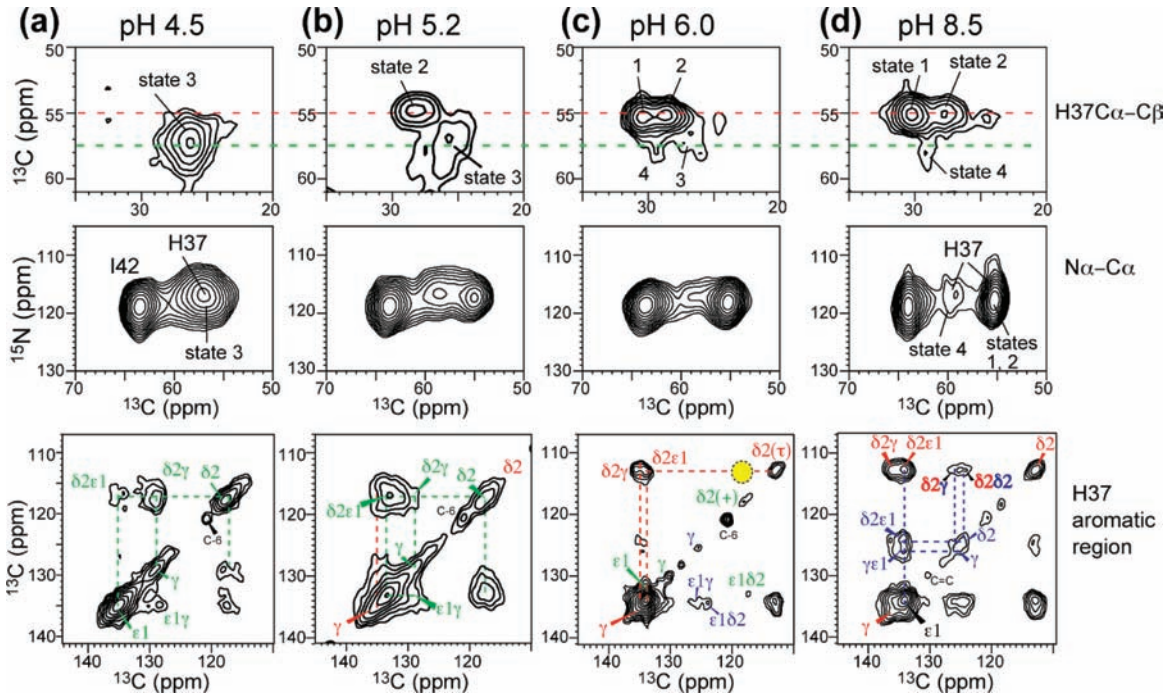

Figure 3. 2D $^{13}C-^{13}C$ and $^{15}N-^{13}C$ correlation spectra of His37 at 273 or 243 K as functions of pH. (a) pH 4.5. (b) pH 5.2. (c) pH 6. (d) pH 8.5. States 1−4 denote different backbone conformations.[41] $^{13}C-^{13}C$ 2D correlation spectra were measured with mixing times of 40 or 60 ms. No neutral−cationic $C\delta2(\tau)-C\delta2(+)$ cross-peak was observed (yellow shade) at pH 6.0. A 300 ms spectrum (Figure S3a in the Supporting Information) confirmed the lack of imidazole−imidazolium contact.

strength. The inversion and refocusing of the isotropic chemical shift evolution by the π pulse (i.e., the Hahn echo) was reproduced by inverting the sign of the chemical-shift frequency matrix. Similarly, continuous-wave (CW) dipolar decoupling was approximated by dipolar-frequency inversion by a sequence of 180° pulses spaced by t_{ps},

$$S(t = 2Nt_{ps}) = \frac{1}{2}\vec{1}^{\,T} \cdot \prod_{n=1}^{N} e^{i\left[\bar{\omega}_{CS}(nt_{ps}) + (-1)^n \bar{\omega}_{NH}(nt_{ps})\right]t_{ps} + \bar{\pi}\, t_{ps}} \times \prod_{n=1}^{N} e^{i\left[-\bar{\omega}_{CS}(nt_{ps}) + (-1)^n \bar{\omega}_{NH}(nt_{ps})\right]t_{ps} + \bar{\pi}\, t_{ps}} \cdot \vec{1} \quad (3)$$

thus giving the same average nutation angle as CW decoupling. To speed up the calculation, the products of exponential matrices were evaluated for one rotation period (t_r), and the K^{th} powers of these product matrices were then used to calculate the signal after $2K$ rotor periods. The T_2 relaxation time was obtained from the condition $S(T_2) = e^{-1} = 0.37$.

The location of the T_2 minimum and the change in T_2 with the exchange rate k for purely dipolar modulations under pulsed decoupling were as predicted by Rothwell and Waugh for CW decoupling,[37] while the depth of the T_2 minimum agreed within 20%. In the simulations, we increased the dipolar coupling strength by 10% to match the Rothwell−Waugh curve.

With the frequency and exchange matrices in the same exponents in eq 3, changes in chemical shift and dipolar frequencies occur concomitantly, as in reality. Curves for individual processes, including pure chemical exchange, the MAS effect on the chemical shift anisotropy, and pure dipolar modulation under heteronuclear decoupling, were obtained by setting all other coupling constants or shift differences to zero but otherwise retaining MAS and decoupling.

The chemical shift anisotropy (CSA) is contained in $\omega_{CS,nn}$ in eq 1a. The CSA has been found to have little effect on the overall T_2 relaxation times. This is expected from the theory of MAS, which refocuses the moderate CSA-induced dephasing of the magnetization within a relatively short time, the rotor period. Similarly, the chemical shift asymmetry parameter η has no detectable effect on the total T_2 relaxation time and was set to zero in eq 1a to simplify the simulations. The chemical shift change due to deprotonation was approximated as a change of $2\pi \times 2$ kHz (50 ppm) in the CSA parameter δ_{CSA}. For powder averaging, the angle β in eqs 2a and 2b was varied in 15° steps.

RESULTS

^{15}N NMR Spectra Indicate His37 Protonation and Deprotonation at Physiological pH and Temperature. The ^{15}N and ^{13}C MAS spectra of His37-labeled M2TM in the mildly acidic pH range 7−5 are shown in Figure 2 and Figure S1 in the Supporting Information and compared with spectra at pH 8.5 and 4.5.[23] The ^{15}N chemical shifts are highly sensitive to the protonation state of the imidazole: unprotonated Nδ1 in the τ tautomer and Nε2 in the π tautomer of neutral His resonate at ∼250 ppm, while protonated ^{15}N in cationic and neutral His resonate at 160−190 ppm. 2D correlation spectra (Figure 3) distinguished the protonated Nε2H (176 ppm) and Nδ1H (180 ppm) of cationic His from the protonated Nε2H(τ) and Nδ1H(π) of neutral His at 159 and 170 ppm, respectively. At low temperature, the ^{15}N spectra (Figure 2, left column) show the expected trend of higher cationic His intensity and lower neutral His intensity with decreasing pH. More importantly, at 303−308 K and between pH 5.2 and 7.0, the ^{15}N spectra reveal chemical exchange of the imidazole nitrogens. At pH 5.2, the 250 ppm peak present at 243 K disappeared above 273 K and a new 213 ppm peak appeared at 308 K (Figure 2b). This frequency is halfway between the unprotonated (250 ppm) and protonated (178 ppm) ^{15}N chemical shifts, indicating that it results from equal-population exchange between the two species. Thus, the imidazole rings

dx.doi.org/10.1021/ja2081185 |J. Am. Chem. Soc. 2012, 134, 3703–3713

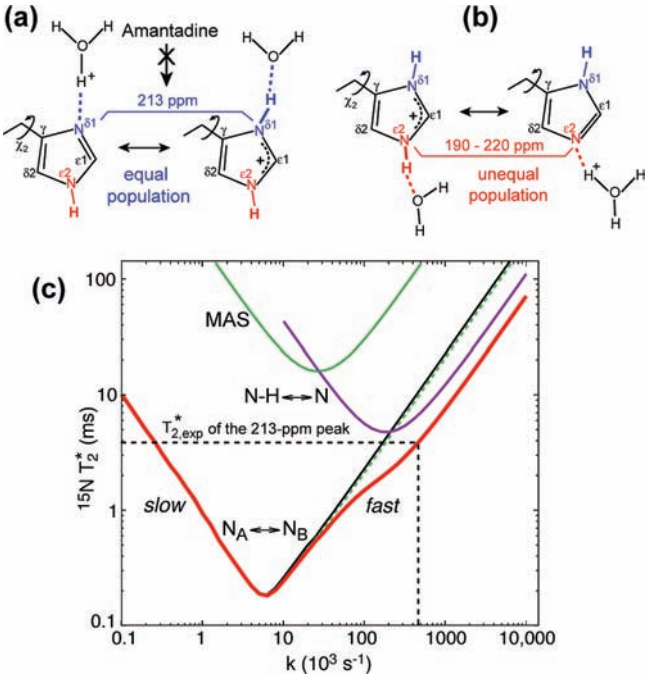

Figure 4. Proton exchange models of His37 and simulations of ^{15}N T_2 to determine the exchange rates. (a) Equal-population Nδ1−Nδ1H exchange, which is suppressed by the drug amantadine. (b) Unequal-population Nε2H−Nε2 exchange. (c) Dependence of the ^{15}N-exchange-induced T_2^* on the exchange rate k. Black line: exchange of isotropic chemical shifts only ($N_A \leftrightarrow N_B$). Green curve at top center: exchange of anisotropic chemical shifts ($\Delta\delta_{CSA}/2\pi$ = 2 kHz) under 7 kHz MAS. Green dashed line: exchange of isotropic ($\Delta\nu$ = 3 kHz) and anisotropic chemical shifts under MAS. Purple curve at top right: N−H dipolar modulation ($\Delta\delta_{NH}/2\pi$ = 9 kHz) under 63 kHz ^{1}H decoupling (N−H ↔ N). Thick red line: full simulation combining all three effects.

undergo protonation and deprotonation at 308 K at a rate much faster than the ^{15}N chemical shift difference ($\Delta\nu$) of ~70 ppm or ~3000 s^{-1}. The protonation and deprotonation events can be attributed to His−water proton exchange but are inconsistent with His−His H-bonding, as we show below. Between Nδ1 and Nε2, the more likely candidate for the 213 ppm exchange peak is Nδ1 (Figure 4a) because chemical shift assignment[23] indicates that Nε2 has higher proton affinities than Nδ1 in His37. Nε2 is the main protonated nitrogen at high pH (Figure 2e) and preserves its protonated chemical shift (159 ppm) from pH 8.5 to 6 before moving downfield at lower pH. Previous bond length measurements indicated a short Nε2−H bond length of 1.03 Å at pH 8.5,[23] also supporting the high proton affinity of Nε2.

In addition to the 213 ppm exchange peak, we also observed a broad-intensity band from 190 to 220 ppm for pH 7 to 5.2 at high temperature. The broadening could be inhomogeneous as a result of a distribution of neutral to charged His ratios, [His]/[HisH$^+$], or homogeneous as a result of exchange at rates comparable to the ^{15}N isotropic chemical shift difference. We measured ^{15}N T_2 relaxation times to distinguish these two possibilities (Figure S2 in the Supporting Information): at pH 5.2, the broad band has a T_2 of 1.7 ms, indicating a homogeneous line width of 4.7 ppm, which is much narrower than the 30 ppm span of the broad peak. Thus, most of the line broadening is inhomogeneous in nature. The center of mass of the broad band is closer to the protonated chemical shift than the unprotonated one, suggesting that the equilibrium is shifted to the protonated state. Since Nε2 has a higher proton affinity, we attribute this broad band to Nε2 exchange (Figure 4b).

Not all of the Nδ1 and Nε2 participate in exchange: the 308 K spectrum at pH 5.2 shows residual intensities at 173 and 185 ppm, indicating that some nitrogens retain their protons most of the time. We attribute the 173 ppm peak to nonexchanging Nε2H and the 185 ppm peak to nonexchanging Nδ1H.

To test whether the ^{15}N exchange peaks result from H-bonding between neutral and cationic His, as proposed in the dimer model,[15,24] we measured 2D ^{13}C−^{13}C correlation spectra at pH 6, where both neutral and cationic His are present (Figure 3c) and where most channels are in the +2 state (see below). If strong H-bonded dimers exist, cross-peaks between neutral and charged side chains would be expected. The Cδ2 peak is well-resolved between the neutral τ tautomer (112 ppm) and cationic imidazolium (118 ppm), thus providing a good probe of intermolecular contacts. The dimer model[15] predicts a Cδ2(τ) to Cδ2(+) distance of 5.9 Å, which is within the distance reach of ^{13}C spin diffusion. Figure 3c and Figure S3 in the Supporting Information show that Cδ2(τ)−Cδ2(+) correlation is absent at mixing times from 40 to 300 ms. In contrast, intertautomer Cδ2(τ)−Cδ2(π) cross-peaks were detected at pH 8.5 within as short a time as 40 ms (Figure 3d), confirming that ^{13}C spin diffusion is able to detect close intermolecular contacts within the His37 tetrad. Thus, the 2D spectra exclude the H-bonded dimer model.

Quantification of Proton Exchange Rates through ^{15}N T_2 Relaxation under ^{1}H Decoupling. To quantify the NH−N exchange rate, we first considered two-site exchange averaging only isotropic chemical shifts. In this scenario, the exchange rate k can be determined from the exchange-induced ^{15}N T_2 relaxation time (T_2^*) and the isotropic shift difference $\Delta\nu$ according to the expression $k = \pi^2\Delta\nu^2T_2^*/2$.[38] For the 213 ppm exchange peak at pH 5.2, we measured an ^{15}N T_2 of 2.8 ms, while the nonexchanging backbone amides have T_2's of ~10 ms (Figure S2 and Table S1 in the Supporting Information). Thus, the exchange-induced T_2^* is 3.9 ± 0.5 ms. With a chemical shift difference of ~3000 Hz, the rate based on the two-site isotropic-shift exchange model is thus 1.8 × 10^5 s^{-1}.

However, for chemical exchange in solids under ^{1}H dipolar decoupling, we need to consider the fact that exchange-induced fluctuations of the ^{15}N−^{1}H dipolar coupling interfere with coherent averaging by ^{1}H decoupling. Similarly, fluctuations of the ^{15}N CSA interfere with time averaging by MAS. We performed numerical simulations to take into account all of these effects quantitatively. An analytical theory for part of this problem, heteronuclear dipolar T_2 relaxation under ^{1}H decoupling, has been described by Rothwell and Waugh.[37] However, the theory was derived for nonspinning solids assuming that isotropic rotational diffusion drives the relaxation, not for two-site exchange in a solid under MAS. To modify that theory for our purpose, we start with the following expression for the time-dependent change in the density operator ρ (eq 7 in ref 37):

$$\frac{d\rho}{dt} = -\sum_{n=\pm 1}[S_zI_n,[S_zI_{-n},\rho]]\int_0^\infty \gamma_I^2\gamma_S^2\hbar^2\left\langle\frac{D_{0,0}^{(2)}(t)}{r^3(t)}\frac{D_{0,0}^{(2)}(t-\tau)}{r^3(t-\tau)}\right\rangle e^{-in\omega_1\tau}\,d\tau \quad (4)$$

where γ_I and γ_S are the gyromagnetic ratios of the I spin (^{1}H) and the heteronuclear spin S (^{15}N), respectively, and $D_{0,0}^{(2)}(t)$ is a Wigner rotation matrix with an angular dependence $[3\cos^2\beta(t) - 1]/2$. In addition to removing the nonsecular terms, we have added an ensemble average over the $D_{0,0}^{(2)}$ terms and moved

dx.doi.org/10.1021/ja2081185 |J. Am. Chem. Soc. 2012, 134, 3703–3713

the distance-dependent term into the integral over τ because the internuclear distance r fluctuates during deprotonation and protonation of the nitrogen. Next, we define a frequency correlation function $C_\omega(\tau)$ as

$$C_\omega(\tau) \equiv \langle \omega(t)\omega(t-\tau)\rangle = {\gamma_I}^2{\gamma_S}^2\hbar^2\left\langle \frac{D^{(2)}_{0,0}(t)}{r^3(t)}\frac{D^{(2)}_{0,0}(t-\tau)}{r^3(t-\tau)}\right\rangle \quad (5)$$

The time evolution of the density operator is related to the correlation function as follows:

$$\frac{d\rho}{dt} = -\sum_{n=\pm 1}[S_zI_n,[S_zI_{-n},\rho]]\int_0^\infty C_\omega(\tau)e^{-in\omega_1\tau}\,d\tau \quad (6)$$

The correlation function decays exponentially toward its asymptotic value $C_\omega(\infty)$ with a time constant τ_C:

$$C_\omega(\tau) = [C_\omega(0) - C_\omega(\infty)]e^{-\tau/\tau_C} + C_\omega(\infty) \quad (7)$$

The constant term in eq 7, $C_\omega(\infty)$, can be disregarded in the following since it contributes to the spectral density only at $\omega = 0$ and not at ω_1.

For exchange between two equally populated sites with frequencies ω_A and ω_B, the correlation function at $\tau = 0$ is $C_\omega(0) = \langle\omega(t)\omega(t)\rangle = \langle\omega^2(t)\rangle = \langle{\omega_A}^2 + {\omega_B}^2\rangle/2$. The frequency at long τ is $(\omega_A + \omega_B)/2$, and thus, $C_\omega(\infty) = \langle(\omega_A + \omega_B)^2/4\rangle$ (for a more stringent derivation, see the Supporting Information). Therefore, eq 6 can be rewritten as

$$\frac{d\rho}{dt} = -\sum_{n=\pm 1}[S_zI_n,[S_zI_{-n},\rho]] \int_0^\infty\langle(\omega_A-\omega_B)^2/4\rangle e^{-\tau/\tau_C}e^{-in\omega_1\tau}\,d\tau \quad (8)$$

Assuming that the N−H vectors in sites A and B are parallel, or that ω_B is negligibly small, we can factorize $\langle(\omega_A - \omega_B)^2\rangle/4$ as

$$\frac{\langle(\omega_A-\omega_B)^2\rangle}{4} = \frac{(\delta_A-\delta_B)^2}{4}\langle[(3\cos^2\beta-1)/2]^2\rangle = \frac{(\delta_A-\delta_B)^2}{4{\delta_A}^2}\langle[\delta_A(3\cos^2\beta-1)/2]^2\rangle \quad (9)$$

where the dipolar coupling constants are $\delta_A = \gamma_I\gamma_S\hbar/{r_A}^3$ and $\delta_B = \gamma_I\gamma_S\hbar/{r_B}^3$ and β is the angle between the N−H vector and the external field B_0. Since the term corresponding to eq 9 in the Rothwell−Waugh theory[37] for isotropic rotational diffusion is $\langle[\delta_A(3\cos^2\beta-1)/2]^2\rangle = {\gamma_I}^2{\gamma_S}^2\hbar^2/5{r_A}^6$, the prefactor $(\delta_A-\delta_B)^2/4{\delta_A}^2$ is the only modification to the Rothwell−Waugh equations. This factor carries through to their eq 10,[37] which in the current context reads

$$\frac{1}{T_2} = \frac{(\delta_A-\delta_B)^2}{4{\delta_A}^2}\frac{{\gamma_I}^2{\gamma_S}^2\hbar^2}{5{r_A}^6}\frac{\tau_C}{1+{\omega_1}^2{\tau_C}^2} \quad (10)$$

For $\delta_A = 2\pi \times 10$ kHz for an N−H bond and $\delta_B = 2\pi \times 1$ kHz for an unprotonated N,

$$\frac{(\delta_A-\delta_B)^2}{4{\delta_A}^2} = \frac{81}{4\times 100} = 0.20 \quad (11)$$

Thus, the dipolar relaxation rate is 5 times smaller than the value obtained if the original Rothwell−Waugh theory is incorrectly applied to the histidine nitrogen undergoing proton exchange. The 5-fold difference arises essentially because half of the time the nitrogen is not protonated and thus has a weak coupling to protons.

Figure 4c shows the calculated ^{15}N T_2^* as a function of the exchange rate k, where all three effects, isotropic chemical shift exchange, CSA modulation under MAS, and N−H dipolar modulation under ^{1}H decoupling, are considered separately and in combination. The T_2^* curves for these processes have minima when the exchange rate is half the relevant frequency ω_X, i.e., the isotropic-shift difference $2\pi\Delta\nu$, the MAS frequency ω_r, and the ^{1}H dipolar decoupling field strength ω_1, as expected for $\omega_X\tau_{min} \approx 1$ and $k = 1/2\tau$. Over a wide range of motional rates, the 3 kHz isotropic-shift exchange is the dominant relaxation mechanism. The effects of the 10 kHz fluctuating N−H dipolar fields are limited by the sufficiently large (63 kHz) ^{1}H decoupling field strength, while the effects of the small (∼2 kHz) ^{15}N CSA fluctuations are strongly suppressed by 7 kHz MAS. The global T_2^* minimum occurs when k matches the isotropic shift difference, while the T_2 contribution from exchange dynamics interfering with ^{1}H decoupling is minor because the nitrogen is protonated only about half the time. The effects of MAS are quite negligible, and the total relaxation rate is quite well approximated as the simple sum of the relaxation rates due to chemical shift exchange and dipolar modulation. The measured T_2^* value of 3.9 ms for the 213 ppm peak translates to a proton exchange rate of $(4.5 \pm 1.0) \times 10^5$ s^{-1}. A second solution in the slow regime, ∼250 s^{-1}, can be excluded by motional narrowing of the ^{15}N spectra, which requires an exchange rate much faster than 3000 s^{-1}. For the broad exchange band assigned to Nε2, the measured T_2^* values at pH 5.2 and 6.0 are 0.9−2.0 ms (Table S1 in the Supporting Information), which correspond to exchange rates of $(1.0 \pm 0.5) \times 10^5$ s^{-1}. These 10^5 s^{-1} rates are about an order of magnitude larger than the proton exchange rates of buffered solutions at similar pH.[39] This difference is expected because the diffusion-limited exchange should be facilitated by the confinement of His37 in the small cavity of the channel.

Proton Dissociation Constants of the His37 Tetrad in M2 Bound to the Virus-Envelope-Mimetic Membrane. The ^{15}N NMR spectra not only reveal the kinetics of proton exchange, but also give rich information on the protonation equilibria of the His37 tetrad in the VM membrane. We integrated the protonated and unprotonated ^{15}N signals at 243 K. The intensity ratios I_{NH}/I_N directly indicate the concentration ratio of neutral to cationic histidines as a function of pH, from which the four equilibrium constants can be calculated (eqs S4 and S5 in the Supporting Information). The intensity ratios were measured at five different pH values for four unknown pK_a's, and thus, the problem was overdetermined. The 243 K ^{15}N spectra (Figure 2, left column) were used for peak integration because the low-temperature intensities are minimally affected by motional averaging. We assume that the temperature dependence of the histidine pK_a values can be neglected because it should be largely canceled by the temperature dependence of the buffer pK_a, which has a similar trend and magnitude. Figure 5a plots the I_{NH}/I_N ratios as a function of pH, and the corresponding [His]/[HisH$^+$] ratios are shown in Figure 5b. Fitting the latter yielded four pK_a's for the His37 tetrad in the VM-membrane-bound M2TM: 7.6 ± 0.1, 6.8 ± 0.1, 4.9 ± 0.3, and 4.2 ± 0.6 (gray vertical lines), where the error bars include both systematic uncertainties in the sample pH and the propagated random uncertainties in the intensity ratios (Table S2 in the Supporting Information). For comparison, the pK_a's of the peptide in DMPC/DMPG bilayers have

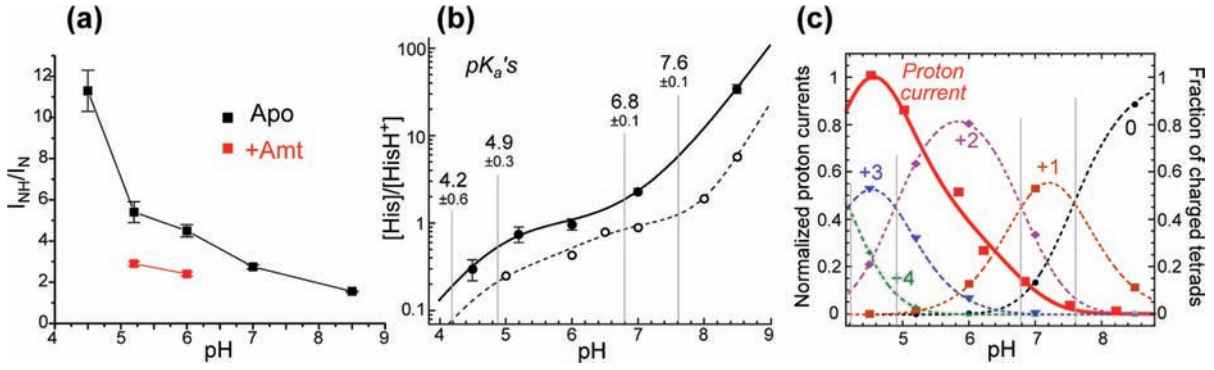

Figure 5. Protonation equilibria of the His37 tetrad in VM-membrane-bound M2TM. (a) I_{NH}/I_N without drug (black) and with drug (red). (b) [His]/[HisH$^+$] ratios (●) as a function of pH and the best-fit curve (solid line), from which the four pK_a's were obtained. For comparison, the [His]/[HisH$^+$] ratios reported previously for DMPC/DMPG-bound M2TM (○ and dashed line)[24] are also shown. (c) Proton currents of Udorn M2 (red ■)[7] and normalized populations of all five charge states (symbols and dotted lines) as a function of pH. The best fit of the proton currents (solid red line) was obtained using relative time-averaged unitary conductances of 1.9 ± 0.2, 5.5 ± 0.7, and 0.4 ± 1.6 for the +2, +3, and +4 channels, respectively, and 0 for the +1 and neutral channels.

been reported[24] as 8.2, 8.2, 6.3 and <5 on the basis of a different set of measured [His]/[HisH$^+$] values (Figure 5b, dotted line). Therefore, in comparison with the previous model-membrane result, the four histidines are protonated at lower pH and the first two protonation steps are resolved in the cholesterol-rich VM membrane. The methods for extracting pK_a's differ between the two studies. We obtained [His]/[HisH$^+$] ratios from the relative intensities of unprotonated and protonated ^{15}N signals, which are resolved by more than 70 ppm. The different ^{1}H−^{15}N CP efficiencies of N and NH signals were taken into account by calibration using a model compound (Figure S4 in the Supporting Information), so the intensity ratio accurately reflects the relative amounts of unprotonated and protonated nitrogens. In comparison, the previous model-membrane study[24] obtained [His]/[HisH$^+$] ratios by deconvolution of the broad protonated ^{15}N peak into multiple components, which had large uncertainties due to significant exchange broadening of these peaks at the temperature of the experiments. Apart from experimental uncertainties, the pK_a differences may also reflect real differences in the protonation equilibria of M2TM in the two lipid membranes: the anionic DMPG used in the previous study may increase the local concentration of protons on the bilayer surface, thus increasing the apparent pK_a values.

To relate the His pK_a's to electrophysiological data, we fit the proton currents of Udorn and Weybridge M2 (Table S3 in the Supporting Information)[7,40] as the population-weighted sum of the time-averaged unitary currents. We assumed that the equilibrium populations of the four charge states, which are fully determined by the pK_a's, were applicable to the kinetic conditions under which the proton currents were measured. The charge-state populations of the channels, N_i, are related to the acid dissociation constants K_i according to

$$\begin{aligned} N_{+4} &= [H^+]^4/\Sigma \\ N_{+3} &= [H^+]^3K_1/\Sigma \\ N_{+2} &= [H^+]^2K_1K_2/\Sigma \\ N_{+1} &= [H^+]K_1K_2K_3/\Sigma \\ N_0 &= K_1K_2K_3K_4/\Sigma \end{aligned} \quad (12)$$

where the normalization constant is $\Sigma = [H^+]^4 + [H^+]^3K_1 + [H^+]^2K_1K_2 + [H^+]K_1K_2K_3 + K_1K_2K_3K_4$. Figure 5c plots the populations of the five charge states of the channel as functions of pH. As expected, the more cationic tetrads are populated at lower pH, and the intersections of the population curves of two neighboring charge states correspond to the pK_a's (gray vertical lines).

The proton current at a certain pH is the electrochemical potential multiplied by the sum of the products of the population N_i, the open probability $P_{o,i}$, and the unitary conductance g_i for each charge state i:

$$I = (V - E_H)\sum_{i=0}^{+4} N_i P_{o,i} g_i \quad (13)$$

The electrochemical potential, which provides the driving force for proton conduction, is the difference between the applied voltage V and the Nernst potential E_H. The latter results from the pH difference between the inside and outside of the membrane: $E_H = 2.303RT(pH_{in} - pH_{out})/F$, where R is the gas constant, T is the temperature, and F is the Faraday constant. The product of the the unitary conductance and the open probability is the time-averaged single-channel conductance $\bar{g}_i$:

$$\bar{g}_i = P_{o,i} g_i \quad (14)$$

We fit two sets of proton current data. Wang et al[7] reported proton currents of Udorn M2 using an applied voltage of −120 mV, pH_{in} = 7.5, and pH_{out} = 4.5−8.2. Chizhmakov et al[40] reported the chord conductance $g = I/(V - E_H)$ for the Weybridge strain of M2 using an applied voltage of −60 mV, pH_{in} = 7.4, and pH_{out} = 4.0−7.2 (Table S3 in the Supporting Information). The latter data set can be fit using the equation

$$\frac{g}{g_{max}} = \sum_{i=0}^{+4} N_i P_{o,i} g_i = \sum_{i=0}^{+4} N_i \bar{g}_i \quad (15)$$

Figure 5c shows the Udorn M2 proton current data (red squares) as a function of pH. The current reaches a maximum at the lowest pH of 4.5 and is close to zero above neutral pH. Qualitatively, this already indicates that the neutral and +1 tetrads, which are predominantly populated above pH 7, conduct few protons, while the +3 channels, whose population curve has a very similar pH dependence as the functional curve with a maximum near pH 4.5, are chiefly responsible for proton conduction. Quantitative fitting of the proton current curve using the charge-state populations gave relative $\bar{g}_i$ values of

dx.doi.org/10.1021/ja2081185 |J. Am. Chem. Soc. 2012, 134, 3703–3713

1.9 ± 0.2, 5.5 ± 0.7, and 0.4 ± 1.6 for the +2, +3, and +4 charge states, respectively, and 0 for the neutral and +1 states, confirming that the +3 channel has the highest time-averaged unitary conductance. Importantly, these relative $\bar{g}_i$ values were obtained without a priori assumptions about whether a given charge state conducts or not. The same qualitative trend was observed by fitting the conductance of Weybridge M2,[40] which yielded relative $\bar{g}_i$ values of 0.47 ± 0.07, 1.41 ± 0.24, and 0.70 ± 0.25 for the +2, +3, and +4 states, respectively (Figure S5a in the Supporting Information). Both sets of proton current data indicate that the +2 state has nonvanishing proton fluxes that are 2−3-fold smaller than for the +3 state (Figure S5b). The time-averaged unitary conductance of the +4 channel has large uncertainties due to the difficulty of measuring whole-cell currents at the lowest pH.

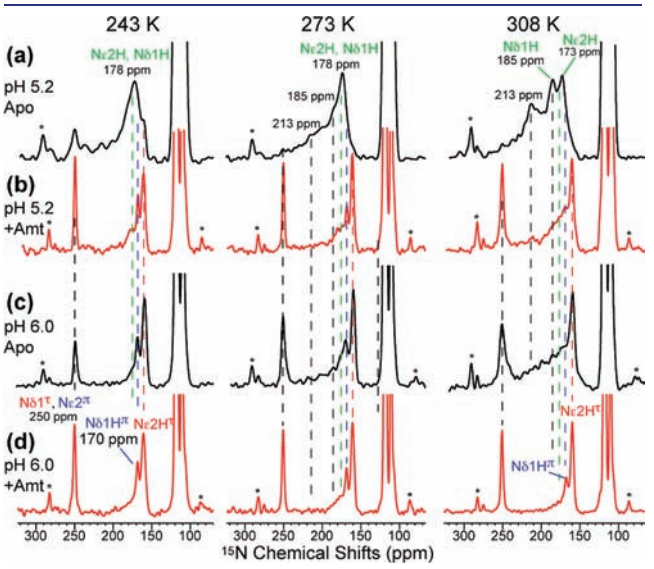

Figure 6. ^{15}N CP-MAS spectra of His37 in apo (a, c) and drug-bound (b, d) M2TM at (a, b) pH 5.2 and (c, d) pH 6.0 at 243, 273, and 308 K. Drug binding increased the unprotonated peak intensity at 250 ppm and reduced the exchange intensities.

pH-Dependent Backbone Conformational Changes. 2D ^{13}C−^{13}C and ^{15}N−^{13}C correlation spectra (Figure 3) revealed not only His37 side-chain structure but also backbone conformational changes as a function of pH. In general, the His37 Cα chemical shift increased and the Cβ chemical shift decreased with decreasing pH, indicating that the His37 backbone became more helical.[41] Four backbone conformations can be identified over the whole pH range. At pH 8.5, three nonideal helical conformations with distinct Cα, Cβ, and ^{15}N chemical shifts were resolved (Figure 3d), whereas at low pH, the peaks were broadened and shifted to more ideal helical chemical shifts (Figure 3a). We designate these conformations as states 1−4, of which states 1−3 had been recently reported.[41] These states do not correlate in a simple way to the charge states of the channel, since the M2TM conformation is also affected by the lipid membrane. At pH 5.2, the Cα−Cβ cross-peaks indicate that the nonideal helical state 2 coexists with the broadly distributed ideal helical state 3 without fast exchange between them, since the two peaks appear at their limiting frequencies from 273 K (Figure 3b) to 308 K (Figure S3b in the Supporting Information). In view of the ^{13}C chemical shift differences of ~300 Hz, any conformational exchange must be much slower than 300 s^{-1}. Decreasing the pH to 4.5 left only the broad peak for state 3, which has a shorter ^{15}N T_2 than the other conformations (Table S1 in the Supporting Information), indicating that the low-pH peptide undergoes small-amplitude fluctuations and samples a broad conformational space. The fact that the average conformation of the low-pH peptide is more ideally helical suggests that the splayed-open packing of the C-terminal half of the helix in the low-pH crystal structure[11] is present in bilayers, even though the crystal structure was determined using detergent-solubilized M2TM. Taken together, the 2D spectra indicate that multiple backbone conformations exist from pH 8.5 to 4.5 but that no fast interconversion occurs between the two main conformations at physiological acidic pH on the sub-10 ms time scale in the VM membrane.

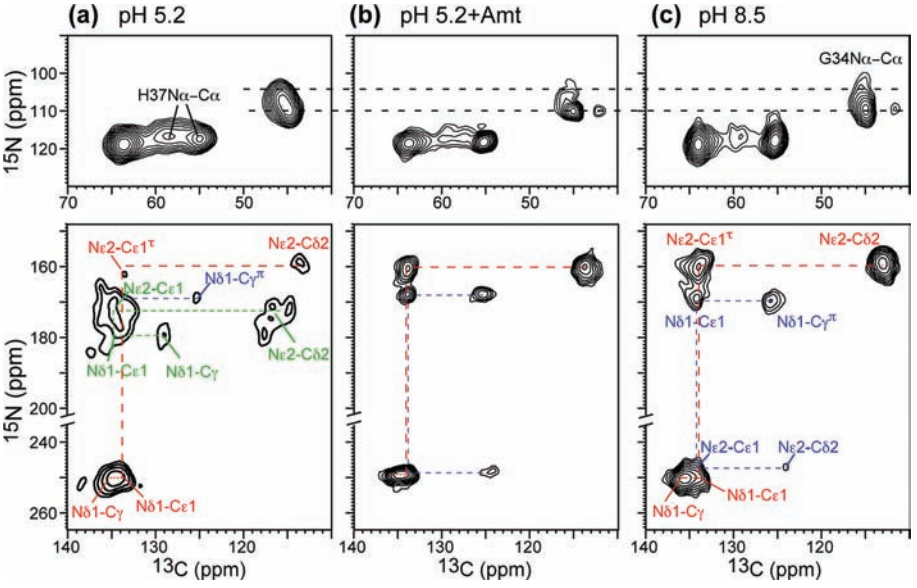

Figure 7. 2D ^{15}N−^{13}C correlation spectra of His37 and Gly34-labeled M2TM without and with Amt at 243 K. (a) pH 5.2 without drug. (b) pH 5.2 with Amt. (b) pH 8.5 without drug. Top row: backbone N−Cα region. Bottom row: imidazole side-chain region. The drug-bound spectrum at pH 5.2 resembles the drug-free spectrum at pH 8.5.

dx.doi.org/10.1021/ja2081185 |J. Am. Chem. Soc. 2012, 134, 3703–3713

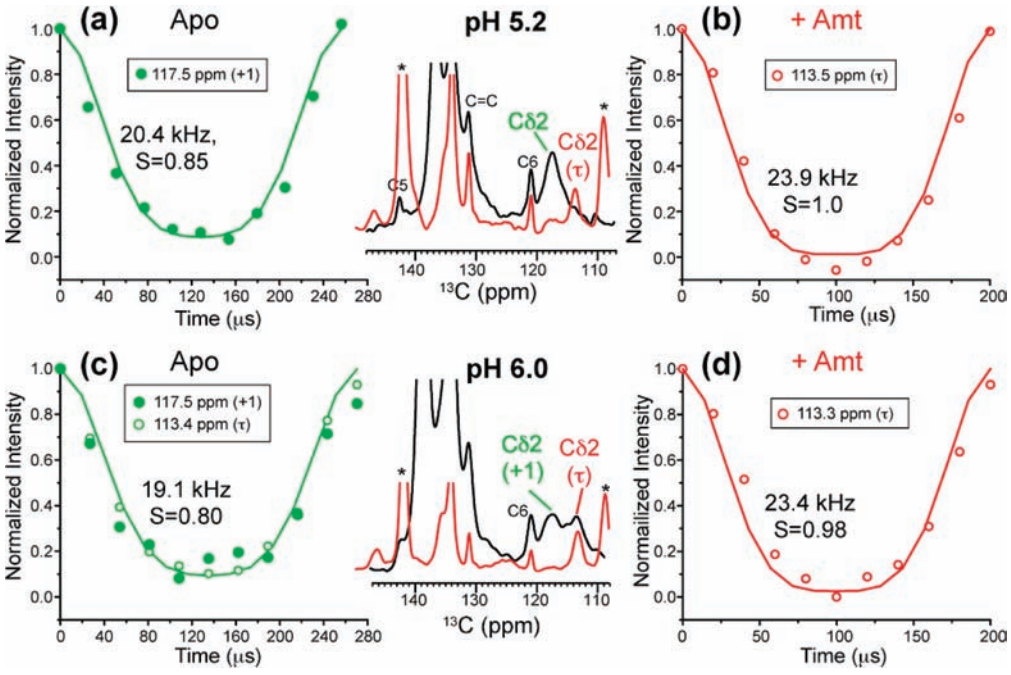

Figure 8. His37 side-chain dynamics at mildly acidic pH and 308 K from Cδ2−H dipolar couplings. (a) Apo peptide at pH 5.2. (b) Amt-bound peptide at pH 5.2. (c) Apo peptide at pH 6. (d) Amt-bound peptide at pH 6. The aromatic regions of the ^{13}C spectra of the drug-free (black) and drug-bound (red) samples are compared in the middle column. The data were measured under (a, c) 3.9 and 3.7 kHz MAS and (b, d) 5 kHz MAS. The best-fit C−H dipolar coupling value and the corresponding bond order parameter are indicated for each curve.

Effects of Amt Binding on His37 Proton Exchange and Motion. If His37−water proton exchange is essential for proton conduction, then Amt binding should suppress this exchange and reestablish the I_{NH}/I_N ratios. Indeed, the ^{15}N spectra of drug-bound M2TM at pH 6.0 and 5.2 (Figure 6) showed a significant increase in the 250 ppm intensity, suppression of the 213 ppm peak, and reduction in the 190−220 ppm intensity. 2D $^{15}N-^{13}C$ correlation spectra confirmed that the drug-bound peptide at pH 5.2 has similar conformation as the apo peptide at pH 8.5 (Figure 7), indicating that Amt binding, although occurring at Ser31,[10] inhibits Nδ1 protonation at His37. Recent water−protein ^1H spin diffusion experiments showed that Amt binding dehydrated the N-terminal pore and reduced the water-exposed surface area of the protein by 2-fold.[42] Thus, inhibition of His37 protonation likely results from reduced accessibility to water. The effect of Amt on the Nε2H−Nε2 exchange is weaker, as the 190−220 ppm intensity is partially retained (Figure 6b). This is consistent with the presence of water C-terminal to His37, as seen in both SSNMR data[23] and the 1.65 Å crystal structure.[16] When Nε2 is unprotonated, Nδ1 must be protonated, giving the π tautomer. Indeed, the 170 ppm peak of the π tautomer is stronger in the drug-bound spectra than the apo spectra. The higher intensity of the 250 ppm peak (Figure 6b, d), which corresponds to a pK_a reduction, is also consistent with previous results for DMPC/DMPG-bound M2TM.[43] Amt binding at pH 5.2 also perturbed the Gly34 conformation by shifting it to a less helical state, as seen in the 2D $^{15}N-^{13}C$ correlation spectra (Figure 7b),[41] indicating that the low-pH drug-complexed peptide adopts a conformation similar to the kinked helix of the apo peptide at high pH.

In the drug-free low-pH channel, the His37 side chain undergoes small-angle reorientations[23] that were proposed to orient the imidazole nitrogens to water molecules for proton transfer. To test whether this motion persists in the presence of the drug, we measured Cδ2−H dipolar couplings of the drug-bound M2TM at pH 5.2 and 6.0. Indeed, the Cδ2−H dipolar coupling reached the rigid limit at 308 K in the Amt-bound state, in contrast to the apo state at the same pH (Figure 8). Thus, the imidazolium ring motion is inhibited by Amt.

DISCUSSION

These ^{15}N NMR data, measured at physiological temperature, pH, and membrane composition, provide rich insights into the proton conduction mechanism of the influenza M2 channel. The imidazole nitrogens protonate and deprotonate at rates of 10^5 s^{-1}, averaging the ^{15}N isotropic chemical shifts. These rates were determined from CP-MAS spectra, which have rarely been used for quantitative kinetic analysis of systems undergoing chemical exchange because the analysis has been perceived as complex and difficult: in addition to the stochastic chemical exchange process, two separate coherent averaging processes are present, dipolar decoupling and magic-angle spinning, on time scales that are not sufficiently separate to make the problem easily reducible. Our novel analysis overcomes this difficulty and takes all these dynamic processes into account.

The 10^5 s^{-1} proton exchange rate is about an order of magnitude larger than the proton transfer rates in buffered solutions,[39] indicating that His37 confinement in the water-filled pore speeds up the diffusion-limited proton transfer. The His37 proton exchange rate is consistent with the ring reorientation rate estimated from motionally averaged dipolar couplings,[23] supporting the proposal that ring reorientation is synchronized with, and facilitates, proton transfer. The measured proton exchange rate is significantly higher than the time-averaged unitary proton flux of M2 from whole-cell patch-clamp and liposome experiments.[5,6,44]

dx.doi.org/10.1021/ja2081185 |J. Am. Chem. Soc. 2012, 134, 3703–3713

This is expected because the NMR-detected exchange rate includes futile exchanges, where a proton may be transferred to and from His37 repeatedly without exiting the channel, which is likely due in part to the action of the gating residue Trp41.[45,46] It should be noted that the reported open probabilities and unitary conductances of M2 vary widely because M2 is not a voltage- or ligand-gated channel and its conductance is too small to be measured accurately.

The His37 protonation and deprotonation require H-bonding with water: Amt binding in the N-terminal pore, which dehydrates the channel,[42] completely suppressed the 213 ppm exchange peak (Figure 6b). In comparison, the Nε2 exchange intensity is partially retained in the presence of the drug, consistent with the retention of water C-terminal to His37.[23] The water−His37 exchange agrees well with the observed water clusters above and below the His37 tetrad in the pH 6.5 crystal structure.[16]

The absence of neutral−cationic histidine cross-peaks in the 2D spectra (Figure 3c) rules out the existence of strong H-bonds between histidines. In addition, the H-bonded dimer model requires the His37 χ_2 angle to be 90°,[15] which contradicts the χ_2 angle of 180° measured in the lipid bilayer by SSNMR[23] and in the detergent by crystallography.[16] The 180° χ_2 angle points Nδ1 toward the N-terminus of the pore, supporting H-bonding with water rather than to a neighboring His.

The four pK_a's for the viral-membrane bound M2TM yielded the populations of the five charge states as a function of pH. Using these populations, we fit the proton conductances from two independent functional studies[7,40] to obtain the relative conductances of the charge states. Both fits indicated that the +3 channel has the highest time-averaged unitary conductance and is thus chiefly responsible for M2's proton channel activity (Figure 5c). The high $\bar{g}_{+3}$ can be due to a large open probability, a high intrinsic unitary conductance, or a combination of the two. Although the +2 channel has a lower $\bar{g}$, its population is the largest in the physiological pH range, so it may be important for proton storage before full channel activation, as proposed recently.[16] The +4 state has a smaller $\bar{g}$ than the +3 channel, even though it must have the highest open probability,[46] suggesting that its intrinsic conductance g_{+4} is low. This is reasonable because the +4 tetrad exerts the largest repulsion with the proton, which should cause a higher energy barrier for proton transport than in the case of the +3 state, as predicted by calculations.[20]

In the VM membrane, M2TM does not exhibit large-amplitude backbone conformational interconversion on the sub-10 ms time scale at physiological pH, contradicting the transporter model.[25,26] Instead, we observed broad ^{15}N line widths and short T_2's for the state that dominates at low pH (state 3), suggesting that the functionally relevant motions are small-amplitude fluctuations around a relatively ideal helical conformation. Although the VM membrane is relatively ordered because of the presence of cholesterol and sphingomyelin, the TM peptide retains its drug-binding ability in this membrane.[47] Thus, the lack of large-scale transport-synchronized backbone motion cannot be attributed to the lack of conformational flexibility of the helical bundle. Instead, our data suggest a different type of protein backbone motion, entailing much smaller amplitudes, for proton transport.

CONCLUSION

In conclusion, these solid-state NMR data provide definitive evidence of His37 protonation and deprotonation at physiological acidic pH. The $(1.0-4.5) \times 10^5$ s^{-1} proton transfer between His and water is synchronized with imidazole ring reorientations. The +3 channel has the highest time-averaged unitary conductance, defining the activated channel. We suggest that Trp41, through interactions with His37, reduces the high His37 proton exchange rate to the much smaller time-averaged proton flux. The lack of close contact between neutral and charged histidines rules out the H-bonded dimer model, while the lack of large-amplitude backbone conformational changes in the VM membrane modifies the transporter model. These findings support the shuttle mechanism, where protons from water molecules bind and unbind His37 on the microsecond time scale, facilitated by ring reorientation and small-amplitude backbone fluctuations.

ASSOCIATED CONTENT

Supporting Information. Additional equations for the correlation function, pK_a analysis, tables of ^{15}N T_2 values, histidine intensity quantification, proton current data, and NMR spectra. This material is available free of charge via the Internet at http://pubs.acs.org.

AUTHOR INFORMATION

Corresponding Author
mhong@iastate.edu

ACKNOWLEDGMENT

This work was funded by NIH Grant GM088204 and NSF Grant MCB-0543473.

REFERENCES

(1) Cady, S. D.; Luo, W. B.; Hu, F.; Hong, M. *Biochemistry* **2009**, *48*, 7356–7364.
(2) Pinto, L. H.; Lamb, R. A. *J. Biol. Chem.* **2006**, *281*, 8997–9000.
(3) Rossman, J. S.; Jing, X.; Leser, G. P.; Lamb, R. A. *Cell* **2010**, *142*, 902–913.
(4) Schroeder, C.; Heider, H.; Möncke-Buchner, E.; Lin, T. I. *Eur. Biophys. J.* **2005**, *34*, 52–66.
(5) Lin, T. I.; Schroeder, C. *J. Virol.* **2001**, *75*, 3647–3656.
(6) Mould, J. A.; Li, H. C.; Dudlak, C. S.; Lear, J. D.; Pekosz, A.; Lamb, R. A.; Pinto, L. H. *J. Biol. Chem.* **2000**, *275*, 8592–8599.
(7) Wang, C.; Lamb, R. A.; Pinto, L. H. *Biophys. J.* **1995**, *69*, 1363–1371.
(8) Balannik, V.; Carnevale, V.; Fiorin, G.; Levine, B. G.; Lamb, R. A.; Klein, M. L.; DeGrado, W. F.; Pinto, L. H. *Biochemistry* **2010**, *49*, 696–708.
(9) Wang, C.; Takeuchi, K.; Pinto, L. H.; Lamb, R. A. *J. Virol.* **1993**, *67*, 5585–5594.
(10) Cady, S. D.; Schmidt-Rohr, K.; Wang, J.; Soto, C. S.; DeGrado, W. F.; Hong, M. *Nature* **2010**, *463*, 689–692.
(11) Stouffer, A. L.; Acharya, R.; Salom, D.; Levine, A. S.; Di Costanzo, L.; Soto, C. S.; Tereshko, V.; Nanda, V.; Stayrook, S.; DeGrado, W. F. *Nature* **2008**, *451*, 596–599.
(12) Jing, X.; Ma, C.; Ohigashi, Y.; Oliveira, F. A.; Jardetzky, T. S.; Pinto, L. H.; Lamb, R. A. *Proc. Natl. Acad. Sci. U.S.A.* **2008**, *105*, 10967–10972.
(13) Rosenberg, M. R.; Casarotto, M. G. *Proc. Natl. Acad. Sci. U.S.A.* **2010**, *107*, 13866–13871.
(14) Cady, S. D.; Mishanina, T. V.; Hong, M. *J. Mol. Biol.* **2009**, *385*, 1127–1141.
(15) Sharma, M.; Yi, M.; Dong, H.; Qin, H.; Peterson, E.; Busath, D.; Zhou, H. X.; Cross, T. A. *Science* **2010**, *330*, 509–512.

(16) Acharya, A.; Carnevale, V.; Fiorin, G.; Levine, B. G.; Polishchuk, A.; Balannick, V.; Samish, I.; Lamb, R. A.; Pinto, L. H.; DeGrado, W. F.; Klein, M. L. *Proc. Natl. Acad. Sci. U.S.A.* **2010**, *107*, 15075–15080.
(17) Schnell, J. R.; Chou, J. J. *Nature* **2008**, *451*, 591–595.
(18) Agmon, N. *Chem. Phys. Lett.* **1995**, *244*, 456–462.
(19) Sansom, M. S. P.; Kerr, I. D.; Smith, G. R.; Son, H. S. *Virology* **1997**, *233*, 163–73.
(20) Chen, H.; Wu, Y.; Voth, G. A. *Biophys. J.* **2007**, *93*, 3470–3479.
(21) Okada, A.; Miura, T.; Takeuchi, H. *Biochemistry* **2001**, *40*, 6053–6060.
(22) Pinto, L. H.; Dieckmann, G. R.; Gandhi, C. S.; Papworth, C. G.; Braman, J.; Shaughnessy, M. A.; Lear, J. D.; Lamb, R. A.; DeGrado, W. F. *Proc. Natl. Acad. Sci. U.S.A.* **1997**, *94*, 11301–11306.
(23) Hu, F.; Luo, W.; Hong, M. *Science* **2010**, *330*, 505–508.
(24) Hu, J.; Fu, R.; Nishimura, K.; Zhang, L.; Zhou, H. X.; Busath, D. D.; Vijayvergiya, V.; Cross, T. A. *Proc. Natl. Acad. Sci. U.S.A.* **2006**, *103*, 6865–6870.
(25) Khurana, E.; Dal Peraro, M.; DeVane, R.; Vemparala, S.; DeGrado, W. F.; Klein, M. L. *Proc. Natl. Acad. Sci. U.S.A.* **2009**, *106*, 1069–1074.
(26) Polishchuk, A. L.; Lear, J. D.; Ma, C.; Lamb, R. A.; Pinto, L. H.; DeGrado, W. F. *Biochemistry* **2010**, *49*, 10061–10071.
(27) Decoursey, T. E. *Physiol. Rev.* **2003**, *83*, 475–579.
(28) Luo, W.; Cady, S. D.; Hong, M. *Biochemistry* **2009**, *48*, 6361–6368.
(29) Cady, S. D.; Hong, M. *Proc. Natl. Acad. Sci. U.S.A* **2008**, *105*, 1483–1488.
(30) Cady, S. D.; Hong, M. *J. Biomol. NMR* **2009**, *45*, 185–196.
(31) Takegoshi, K.; Nakamura, S.; Terao, T. *Chem. Phys. Lett.* **2001**, *344*, 631–637.
(32) Hong, M.; Griffin, R. G. *J. Am. Chem. Soc.* **1998**, *120*, 7113–7114.
(33) Munowitz, M. G.; Griffin, R. G.; Bodenhausen, G.; Huang, T. H. *J. Am. Chem. Soc.* **1981**, *103*, 2529–2533.
(34) Rhim, W.-K.; Elleman, D. D.; Vaughan, R. W. *J. Chem. Phys.* **1973**, *59*, 3740–3749.
(35) Bielecki, A.; Kolbert, A. C.; Levitt, M. H. *Chem. Phys. Lett.* **1989**, *155*, 341–346.
(36) Abragam, A. *Principles of Nuclear Magnetism*; Clarendon Press: Oxford, U.K., 1961.
(37) Rothwell, W. P.; Waugh, J. S. *J. Chem. Phys.* **1981**, *74* 2721–2732.
(38) Harris, R. K. *Nuclear Magnetic Resonance Spectroscopy: a Physicochemical View*; Longman Scientific & Technical: Harlow, England, 1986.
(39) Luz, Z.; Meiboom, S. *J. Am. Chem. Soc.* **1963**, *85*, 3923–3925.
(40) Chizhmakov, I. V.; Geraghty, F. M.; Ogden, D. C.; Hayhurst, A.; Antoniou, M.; Hay, A. J. *J. Physiol.* **1996**, *494*, 329–336.
(41) Hu, F.; Luo, W.; Cady, S. D.; Hong, M. *Biochim. Biophys. Acta* **2011**, *1808*, 415–423.
(42) Luo, W.; Hong, M. *J. Am. Chem. Soc.* **2010**, *132*, 2378–2384.
(43) Hu, J.; Riqiang, F.; Cross, T. A. *Biophys. J.* **2007**, *93*, 276–283.
(44) Moffat, J. C.; Vijayvergiya, V.; Gao, P. F.; Cross, T. A.; Woodbury, D. J.; Busath, D. D. *Biophys. J.* **2008**, *94*, 434–445.
(45) Tang, Y.; Zaitseva, F.; Lamb, R. A.; Pinto, L. H. *J. Biol. Chem.* **2002**, *277*, 39880–39886.
(46) Zhou, H. X. *Biophys. J.* **2011**, *100*, 912–921.
(47) Cady, S. D.; Wang, T.; Hong, M. *J. Am. Chem. Soc.* **2011**, *133*, 11572–11579.
(48) Smondyrev, A. M.; Voth, G. A. *Biophys. J.* **2002**, *83*, 1987–1996.